The Astrophysical Journal, 632:920–931, 2005 October 20

RADIO AND X-RAY PROFILES IN SUPERNOVA REMNANTS UNDERGOING EFFICIENT COSMIC-RAY PRODUCTION

Donald C. Ellison
Physics Department, North Carolina State University, Box 8202, Raleigh, NC 27695; don_ellison@ncsu.edu

and

Gamil Cassam-Chenaï
Department of Physics and Astronomy, Rutgers University, 136 Frelinghuysen Road, Piscataway, NJ 08854-8019; chenai@physics.rutgers.edu
Received 2005 April 21; accepted 2005 June 30

ABSTRACT

The strong shocks in young supernova remnants (SNRs) should accelerate cosmic rays (CRs), and there is no doubt that relativistic electrons are produced in SNRs. However, direct and convincing evidence that SNRs produce CR nuclei has not yet been obtained and may, in fact, be long in coming if current γ-ray observatories do not see an unambiguous pion-decay feature. Nevertheless, the lack of an observed pion-decay feature does not necessarily mean that CR ions are not abundantly produced since ions do not radiate efficiently. If CR ions are produced efficiently by diffusive shock acceleration (DSA), their presence will modify the hydrodynamics of the SNR and produce morphological effects that can be clearly seen in radiation produced by electrons. We describe in some detail our CR-hydro model, which couples DSA with the remnant hydrodynamics, and the synchrotron emission expected for two distinct parameter sets representing Type Ia and Type II supernovae. Several morphological features emerge in radial profiles, including the forward shock precursor, which are observable with current X-ray observatories and should definitively show whether young SNRs produce CR ions efficiently or not. For the specific case of SN 1006 we conclude, as have others, that the extremely short X-ray scale heights observed near the outer shock argue convincingly for the efficient production of CR ions.

Subject headings: cosmic rays — radio continuum: ISM — shock waves — supernova remnants — X-rays: ISM

1. INTRODUCTION

Collisionless shocks in supernova remnants (SNRs) are believed to produce the majority of Galactic cosmic rays (CRs), at least up to the so-called knee near 10^{15} eV (for a recent review see Hillas 2005). While there is little doubt from the synchrotron interpretation of radio observations that young SNRs produce GeV electrons, and this is probably true for TeV electrons as well from the interpretation of nonthermal X-rays, there is as yet no unambiguous direct evidence that SNRs produce relativistic ions. This is somewhat paradoxical considering that the observed electron-to-proton ratio in CRs is $\sim$0.01 and virtually all models of diffusive particle acceleration in collisionless shocks, the most cited mechanism for producing CRs, predict that ions receive far more energy than electrons (see, e.g., Baring et al. 1999 and references therein). Relativistic electrons, of course, radiate far more efficiently than do ions, leaving open the possibility that a large majority of the energy in relativistic particles in SNRs lies in hard-to-see ions. In this paper we model SNR evolution coupled with the efficient production of CRs (our so-called CR-hydro model; e.g., Ellison et al. 2004) and make a number of predictions for the synchrotron emission from electrons that will be influenced by the presence of otherwise unseen relativistic ions. For a recent summary of observations and models of synchrotron emission in SNRs, see Cassam-Chenaï et al. (2005), who address many of the issues discussed here using a self-similar approach.

In order to power CRs, the shocks in SNRs must be capable of placing $\sim$10% of the supernova (SN) explosion energy into relativistic ions over their lifetime (e.g., Drury 1983; Blandford & Eichler 1987). In fact, the strong shocks in young SNRs may be far more efficient than this (e.g., Ellison 2000; Hughes et al. 2000; Decourchelle et al. 2000) and place enough energy in relativistic particles so that nonlinear feedback effects modify the shock structure, the evolution of the remnant, and the radiative properties (e.g., Berezhko et al. 1996; Decourchelle et al. 2000). As we show below, structural changes produced by DSA translate into changes in synchrotron emission that are large enough to be investigated with modern, high spatial resolution, radio and X-ray observatories. In particular, we calculate the synchrotron emission profiles for typical shell Type Ia and II SN parameters and show how these profiles provide important constraints on the underlying particle acceleration mechanism and magnetic field structure.

Particle acceleration influences the SNR evolution because relativistic particles produce less pressure for a given energy density than do nonrelativistic particles.[1] Therefore, when relativistic particles are produced and/or energetic particles escape from the shock system, the shocked gas becomes more compressible; i.e., it acts as if it has a softer equation of state and the remnant hydrodynamics are modified. The softer effective equation of state means that compression ratios well in excess of 4 can be produced in nonradiative, collisionless shocks (e.g., Blandford & Eichler 1987; Jones & Ellison 1991), and since the energy going into relativistic particles is drawn from the shock-heated thermal population, the temperature of the shocked gas can be much less than that expected from test particle shock

[1] This follows since the ratio of specific heats, Γ, decreases as particles become relativistic and the pressure $P = (\Gamma - 1)e$, where e is the energy density.

acceleration (e.g., Ellison 2000; Decourchelle et al. 2000). In addition to modifying the evolution and the temperature of the shocked gas, changes in the compression of the fluid should result in changes in the compression of the magnetic field implying that synchrotron emission from relativistic electrons will vary strongly with the efficiency of DSA and the orientation and strength of the magnetic field.

Perhaps the most important morphological aspect of this CR-hydro coupling is that the ratio of the forward shock radius, $R_{\rm FS}$, to the radius of the contact discontinuity, $R_{\rm CD}$, may be much less than in the test particle case (see Decourchelle et al. 2000; Ellison et al. 2004). If, as is generally believed, shocks put far more energy into accelerated ions than electrons, it is the efficient production of CR *ions* that reduces $R_{\rm FS}/R_{\rm CD}$ from test particle values. However, since the interaction region between the forward shock (FS) and the contact discontinuity (CD) can be sometimes estimated or determined with modern X-ray telescopes (SN 1006 is an example where the CD is not seen), radiating electrons can reveal the presence of these otherwise unseen relativistic ions.

Another clear morphological prediction from efficient DSA discussed below is that radial profiles of X-ray emission will be strongly peaked and form sheetlike structures at the FS. This effect comes largely from the large shock compression ratios that compress the magnetic field behind the FS and result in severe radiative losses for electrons producing X-rays. Without efficient particle acceleration, the radial profiles of X-rays will be smoother and more closely resemble those for radio emission.

In addition to the radio and X-ray profiles in the interaction region between the CD and the FS, we calculate the emission in the FS precursor. We show that the structure of the X-ray precursor depends strongly on assumptions made for the magnetic field compressibility. If the magnetic field is compressed substantially at the FS, as is likely, the ratio of X-ray intensity immediately upstream of the shock to that at the FS drops dramatically. In this case, line-of-sight projection effects produce profiles that are fully consistent with the extremely short scale heights seen in SN 1006 by Bamba et al. (2003) or Long et al. (2003), even though TeV electrons with long diffusion lengths are present. We conclude for this particular remnant, as did Berezhko et al. (2003), that CR ions are being efficiently produced and their presence is revealed by radiating electrons. We note that the strong magnetic fields we describe at the FS are produced by compression not from magnetic field amplification resulting from CR streaming instabilities, such as predicted by Bell & Lucek (2001). Magnetic field amplification at the FS is not included in our model.

2. CR-HYDRO MODEL

We calculate the hydrodynamic evolution of a SNR coupled to efficient DSA with a radially symmetric model described in detail in Ellison et al. (2004 and references therein). We do not consider CR production at the reverse shock since we assume that the magnetic field in the ejecta is the frozen-in field from the SN progenitor and, as such, will be too small to produce significant particle acceleration or nonthermal emission without large enhancement factors (for a discussion of efficient DSA at reverse SNR shocks see Ellison et al. 2005).

Any realistic model of an SNR will have several parameters for both the environment and the physical processes controlling the evolution and particle acceleration. Here we concentrate on changes in the SNR evolution and emission produced by CR production and choose two fairly distinct models as prototypes, one with parameters typical of Type Ia SNe and the other with parameters like those of Type II SNe. These models differ by the initial density profile in the ejecta[2] and the density and magnetic field profiles in the ambient medium. Within these models, we investigate the effects of varying the CR production efficiency and the magnetic field structure.

2.1. *Type Ia Prototype*

For our Type Ia prototype, we assume that the density profile of the ejecta material is exponential (Dwarkadas & Chevalier 1998), the total ejecta mass is $M_{\rm ej} = 1.4\,M_\odot$, the explosion energy is $E_{\rm SN} = 10^{51}$ ergs, and a uniform ambient medium density, n_p, with a temperature of $T_0 = 10^4$ K. Here n_p is the proton number density and we assume that there is an additional 10% contribution of helium nuclei. We assume that the magnetic field in the interstellar medium (ISM), B_0, is also constant and take $B_0 = 10^{-5}$ G as a default value. We typically view our Type Ia models at an age $t_{\rm SNR} = 400$ yr, similar to the age of Tycho's SNR, when the shock speed is roughly 4000 km s^{-1}.

2.2. *Type II Prototype*

For our Type II prototype, we assume that the initial density profile of the ejecta material is a power law in radius, $\rho_{\rm ej} \propto r^{-n}$, with a constant-density plateau region at small radii (e.g., Arnett 1988). We take $n = 9$ in all of our Type II models. For the total ejecta mass we take $M_{\rm ej} = 2\ M_\odot$, and the explosion energy is set to $E_{\rm SN} = 3 \times 10^{51}$ ergs (Laming & Hwang 2003; Chevalier & Oishi 2003). The density of the pre-SN wind is taken as $\rho_w = Ar^{-2}$, where $A = (dM/dt)/(4\pi v_w)$, dM/dt is the mass-loss rate, and v_w is the wind speed (both assumed constant). We use typical values $v_w = 20$ km s^{-1} and $dM/dt = 2 \times 10^{-5}\ M_\odot$ yr^{-1} (Chevalier & Oishi 2003) and take a constant wind temperature $T_w = 10^4$ K.

Following Chevalier & Luo (1994), we assume that the unshocked magnetic field in the pre-SN wind is

$$B_0(r) = \frac{(\sigma_w v_w\, dM/dt)^{1/2}}{r}, \tag{1}$$

or

$$B_0(r) = 2.6 \left(\frac{\sigma_w}{0.1}\right)^{1/2} \left(\frac{v_w}{10\ {\rm km\ s^{-1}}}\right)^{1/2} \times \left(\frac{dM/dt}{10^{-5}\ M_\odot\ {\rm yr^{-1}}}\right)^{1/2} \left(\frac{r}{1\ {\rm pc}}\right)^{-1}\ \mu{\rm G}, \tag{2}$$

where σ_w is the constant ratio of magnetic field energy density to kinetic energy density in the wind. This expression assumes that the magnetic field is frozen in the constant stellar wind and is only valid in the equatorial plane for distances r much greater than the radius of the pre-SN star.[3] Off the plane, $B(r)$ will fall off more rapidly than $1/r$, but we ignore this effect in our spherically symmetric models. The value of σ_w for stars other than the Sun is not well known, but, for concreteness, we take $\sigma_w = 0.1$. We typically view our Type II models at $t_{\rm SNR} = 400$ yr, to match our Type Ia

[2] Since we do not consider acceleration at the reverse shock, the different ejecta composition in Type Ia and Type II SNe is not important. For a discussion of how composition might influence DSA, see Ellison et al. (2005).

[3] Eq. (1) only applies if the forward shock has not reached the stellar wind termination shock. We assume that the forward shock is within the bubble in all of the examples discussed here.

models and for comparison with SNR Cassiopeia A (Cas A), when the shock speed is roughly 6000 km s^{-1}.

2.3. *Acceleration Model*

For the diffusive shock acceleration process, we use the algebraic model of Berezhko & Ellison (1999) and Ellison et al. (2000) where the injection efficiency is parameterized and the superthermal spectrum, $f(p)$, is a broken power law, $f_{\rm PL}(p)$, with an exponential turnover at high momenta, $f(p) \propto f_{\rm PL}(p) \exp(-p/p_{\rm max})$. The algebraic model solves the nonlinear DSA problem at each time step of the hydro simulation given the shock speed, shock radius, ambient density and temperature, and ambient magnetic field determined in the simulation. With the accelerated distribution, an effective ratio of specific heats is calculated and used in the hydrodynamic equations, completing the coupling between the two (for a full discussion see Ellison et al. 2004).

The injection parameter, $\eta_{\rm inj}$, is the fraction of total protons injected into the DSA process, and values $\eta_{\rm inj} \gtrsim 10^{-4}$ typically yield efficient particle acceleration rates where 10%–99% of the available energy flux goes into relativistic protons.[4] The maximum momentum, $p_{\rm max}$, is determined by setting the acceleration time equal to the SNR age $t_{\rm SNR}$ or by setting the diffusion length of the highest energy particles equal to some fraction, $f_{\rm sk}$, of the shock radius $R_{\rm sk}$, whichever gives the lowest $p_{\rm max}$ (see, e.g., Baring et al. 1999). In all of the models presented here we take $f_{\rm sk} = 0.05$. We assume Bohm diffusion so that the scattering mean free path, λ, is on the order of the gyroradius, r_g, i.e., $\lambda = \eta_{\rm mfp} r_g$ with $\eta_{\rm mfp} = 1$ and $r_g = pc/(qB)$. Here p and q are the particle momentum and charge, respectively, B is the magnetic field at the acceleration site, and c is the speed of light. Note that while our estimate of $p_{\rm max}$ requires a specific assumption for the mean free path, the acceleration model itself only assumes that the scattering mean free path is a strongly increasing function of momentum. In the absence of radiative losses, the maximum kinetic energy particles receive in DSA depends only on the particle charge, and $p_{\rm max}$ is the same for protons and electrons as long as both are relativistic.

2.4. *Synchrotron Emission and Losses*

As the forward shock overtakes fresh ambient medium material, the shock accelerates these particles and produces a nonthermal distribution as described in detail in Ellison et al. (2004, 2005).[5] Once the particle distribution is produced in a shell of material at the shock, it is assumed to remain in that shell as the shell convects and evolves behind the shock. During the evolution, particles experience adiabatic and synchrotron losses, and these losses are calculated as in Reynolds (1998).

In calculating the synchrotron emission and losses, we evolve the magnetic field as described, for example, in Reynolds & Chevalier (1981) or Reynolds (1998). Consider a fluid element that is now at position r with density $\rho(r)$. At an earlier time, this fluid element was shocked at a position r_i where the density immediately behind the shock was ρ_2. The radial and tangential components of the field immediately behind the shock at r_i were B_{2r} and B_{2t}, respectively. If the magnetic flux is frozen in the fluid, the field at the downstream position, r, is given by

$$B^2(r) = B_{2r}^2 \left(\frac{r_i}{r}\right)^4 + B_{2t}^2 \left[\frac{\rho(r)}{\rho_2}\right]^2 \left(\frac{r}{r_i}\right)^2. \quad (3)$$

For the magnetic field configuration across the shock, we assume either that $B_2 = B_0$, as in a parallel shock, or that the field is fully turbulent upstream and, following Völk et al. (2002), set the immediate downstream magnetic field

$$B_2 = \sqrt{\frac{1}{3} + \frac{2r_{\rm tot}^2}{3}} B_0, \quad (4)$$

where $r_{\rm tot}$ is the shock compression ratio.[6] Note that B_2 does not include any amplification effects such as described by Bell & Lucek (2001). Using $B(r)$ obtained in equation (3), the evolution of the electron distribution under combined adiabatic and synchrotron losses is calculated and, at the end of the simulation, the synchrotron emission in each shell is determined as in Baring et al. (1999).[7]

In Figure 1 we show electron momentum phase-space distribution functions, $f(p)$, for a Type Ia SNR model discussed more fully in § 3. In each panel, the dashed line is the distribution calculated immediately after production at the age indicated (i.e., at $t_{\rm shock}$) and the solid line is this distribution at the end of the simulation (i.e., at $t_{\rm SNR} = 1000$ yr) after experiencing adiabatic and synchrotron losses. In the top two panels, the dot-dashed lines show the electron distribution at $t_{\rm SNR} = 1000$ yr when only adiabatic losses are included.

The shock-accelerated distribution, before losses, is a broken power law above a thermal distribution with an exponential cutoff at the maximum momentum (i.e., eq. [12] in Ellison et al. 2000, with $\alpha = 1$). Adiabatic losses affect all particles (shifting the entire distribution to lower momenta, i.e., $p \propto \rho^{1/3}$), while synchrotron losses influence mainly the highest energy electrons. For the parameters of this model, the highest momentum electrons accelerated at early times are strongly depleted and a distinct synchrotron bump is observed just below the sharp maximum momentum cutoff. The thick dotted line in the bottom panel of Figure 1 is the electron distribution at the end of the simulation summed over the interaction region between the contact discontinuity and the forward shock. For comparison we show with the thin dotted line the summed proton distribution at the end of the simulation. For this example, the electron-to-proton ratio at relativistic energies, $(e/p)_{\rm rel}$, is set to 0.01, similar to that of Galactic CRs, and the electron-to-proton temperature ratio immediately behind the shock, T_e/T_p, is set to 1 (for fuller discussion of these parameters see Ellison et al. 2000). The difference between the electron and proton spectra in the bottom panel of Figure 1 illustrates how DSA typically puts far more energy into protons than electrons.

2.5. *Upstream Precursor*

The algebraic acceleration model of Berezhko & Ellison (1999) does not explicitly include the geometry of the shock precursor. However, we can estimate the precursor upstream of the forward

[4] Note the difference between the fraction of protons injected into the acceleration process, $\eta_{\rm inj}$, and the acceleration efficiency. The acceleration efficiency is the fraction of total energy flux going into relativistic particles including all ions and electrons. Given $\eta_{\rm inj}$ and the other shock parameters, the electron spectrum is determined with two additional parameters, the electron-to-proton ratio at relativistic energies, $(e/p)_{\rm rel}$, and the electron-to-proton temperature ratio immediately behind the shock, T_e/T_p (for a full discussion see Ellison et al. 2000).

[5] We ignore preexisting CRs and inject and accelerate only thermal particles overtaken by the shock.

[6] Here and elsewhere the subscript 0 (2) indicates values immediately ahead of (behind) the shock.

[7] In calculating electrons losses, we include inverse Compton losses off the cosmic microwave background radiation as described in Baring et al. (1999). For protons, radiative losses are unimportant for typical SNR magnetic fields.

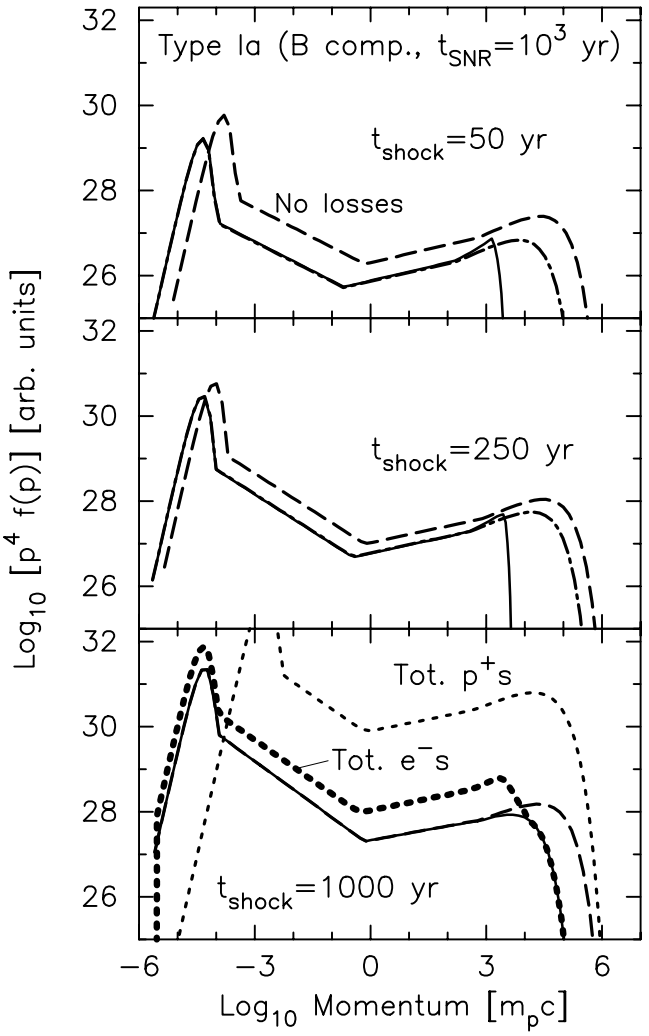

FIG. 1.—Phase-space electron distributions multiplied by p^4. In all panels, the dashed lines were produced, without losses, in shells at the FS at the times indicated, t_{shock}. The solid lines are these distributions at $t_{SNR}=10^3$ yr with adiabatic and synchrotron losses taken into account, and, in the top two panels, the dot-dashed lines are these distributions at $t_{SNR}=10^3$ yr with only adiabatic losses included. The thick (thin) dotted line in the bottom panel is the total electron (proton) distribution, with all losses, from the interaction region between the CD and the FS at t_{SNR}. The magnetic field is compressed at the shock as in eq. (4) and $\eta_{inj}=10^{-3}$.

shock in the following way. At any particular time, the proton distribution in the outermost shell, $f_p(p)$, produces the precursor. We assume that the protons of momentum p in this distribution "feel" a flow speed $u(z)$ and magnetic field $B(z)$, where z is the diffusion length, $L_D(p)$, measured upstream from the FS. The diffusion length $L_D(p)=\kappa(p)/u(z)$, where $\kappa=\lambda v/3$ is the diffusion coefficient, v is the particle speed, and $u(z)$ is the flow speed at z measured in a frame at rest with the shock.

We use information from $f_p(p)$ to estimate $u(z)$ and $B(z)$ and obtain $L_D(p)$. Because of shock smoothing, the compression ratio in the FS that produced $f_p(p)$ ranges from the subshock compression, r_{sub}, felt by protons with the superthermal injection momentum p_{inj}, to the overall compression, r_{tot}, felt by protons with p_{max}. Intermediate values of compression, $r(p)$, felt by protons or electrons with momentum p between p_{inj} and p_{max}, can be estimated with a linear extrapolation between $r(p)$ and $\log(pv)$, i.e.,

$$r(p)=r_{sub}+G(p)(r_{tot}-r_{sub}), \tag{5}$$

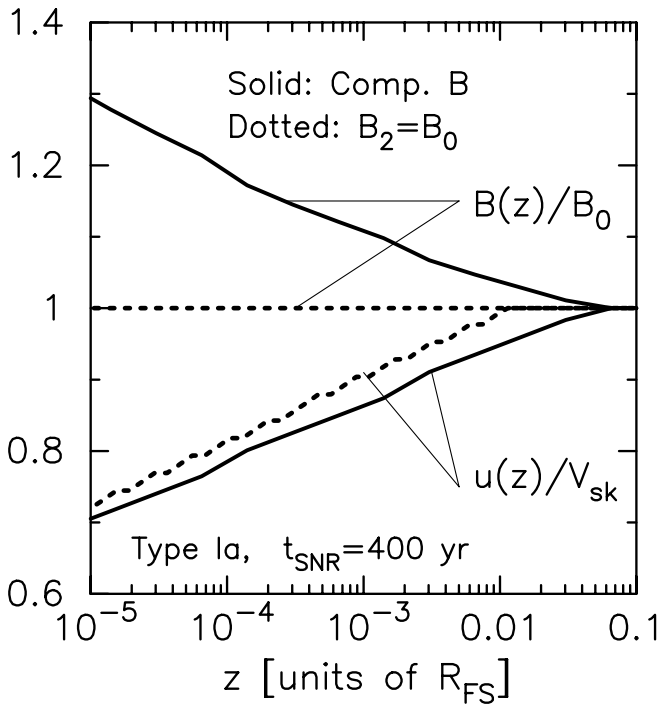

FIG. 2.—Precursor flow speed, u, and magnetic field, B, as functions of z, the distance upstream from the forward shock. The magnetic field is in units of B_0, the far upstream value, and $u(z)$ is in units of the forward shock speed, V_{sk}, measured in the rest frame of the SN. For the Type Ia models shown here, we take $B_0=10\ \mu$G. For our Type II wind models (not shown), we assume that the length scale of the wind is large compared to the precursor scale so that $B(z)$ in eq. (9) is obtained using a constant B_0, where B_0 is the immediate upstream field at t_{SNR}.

where pv is proportional to the diffusion length and

$$G(p)=\frac{\log(pv)-\log(pv)_{inj}}{\log(pv)_{max}-\log(pv)_{inj}}. \tag{6}$$

Here $(pv)_{max}=p_{max}c$, $(pv)_{inj}=p_{inj}v_{inj}$, and v_{inj} is the particle speed corresponding to p_{inj}. Note that since p_{inj} and η_{inj} combine to give a single free injection parameter, the specific value of p_{inj} is unimportant for the results discussed here (for recent work on injection in a semianalytic, nonlinear DSA model see Blasi et al. 2005).

With equation (5), we estimate the flow speed felt by a particle with momentum p as

$$u(z)=V_{sk}\frac{r(p)}{r_{tot}}, \tag{7}$$

and the magnetic field felt by this particle is either

$$B(z)=B_0 \tag{8}$$

or

$$B(z)=B_0\sqrt{\frac{1}{3}+\frac{2}{3}\left[\frac{r_{tot}}{r(p)}\right]^2}, \tag{9}$$

depending on whether the magnetic field is compressed in the precursor (as in eq. [4]) or not. Here V_{sk} is the forward shock speed in the rest frame of the SN.

Given $u(z)$ and $B(z)$, the diffusion length of an electron can be determined and, in a fashion similar to Reynolds (1998), we

assume that electrons of momentum p are distributed upstream from the shock such that

$$f_e(p,\ z) = f_e(p,\ 0)\exp\left\{-z\left[\frac{1}{L_D(p)} + \frac{1}{f_{\rm sk}R_{\rm FS}}\right]\right\}, \quad (10)$$

where $f_e(p,\ 0)$ is the electron distribution in the outermost shell ($z = 0$) at the end of the simulation and $f_{\rm sk}R_{\rm FS}$ sets the distance ahead of the shock where particles freely leave the system. The electron distribution, $f_e(p,\ 0)$, contains the effects of synchrotron and inverse Compton losses that occur during acceleration.

The above relations are approximations in that they ignore the precise form for the smooth precursor flow speed. However, we have verified that the precursor emission is relatively insensitive to this smoothing and that our approximations adequately describe the spatial dependencies important for predicting the synchrotron precursor. Typical results are shown in Figure 2, where the solid lines are for compressed B and the dotted lines are for uncompressed B.

3. RESULTS

3.1. *Radial Emission*

Using the parameters for our Type Ia prototype, we plot in Figure 3 the synchrotron emission as a function of radius for one radio (1–1.4 GHz; *solid lines*) and two X-ray bands (0.1–1 keV, *dashed lines*; 1–10 keV, *dotted lines*). We present four models, two with $\eta_{\rm inj} = 10^{-3}$, which produces very efficient DSA with nearly 100% of the energy flux crossing the shock going into relativistic particles, and two with $\eta_{\rm inj} = 10^{-5}$, which yields essentially a test particle result with less than 1% of the energy flux going into CRs and where the influence of shock-accelerated protons on the hydrodynamics is small. For each $\eta_{\rm inj}$ we show a case with a compressed field (labeled "B comp.") and one with uncompressed field in either the shock or the precursor (labeled "$B_2 = B_0$"). In the compressed field case, we assume, as in Berezhko et al. (2002), that the magnetic field is fully turbulent upstream of the shock and is compressed in the precursor as described by equation (9). The curves are normalized to each energy band's flux at the forward shock.[8]

Figure 4 shows similar results for our Type II prototype where, as in Figure 3, the emission is viewed at $t_{\rm SNR} = 400$ yr.

Comparing these figures, we note the following:

1. The two SN types have very similar profiles at least for the parameters used here. One noticeable difference occurs for the $\eta_{\rm inj} = 10^{-5}$ cases where the Type II radio profiles are flatter than the Type Ia profiles. Later, in association with Figure 9, we show in more detail that changes in $\eta_{\rm inj}$ and other parameters influence the SN types rather differently and may offer help in distinguishing the types.

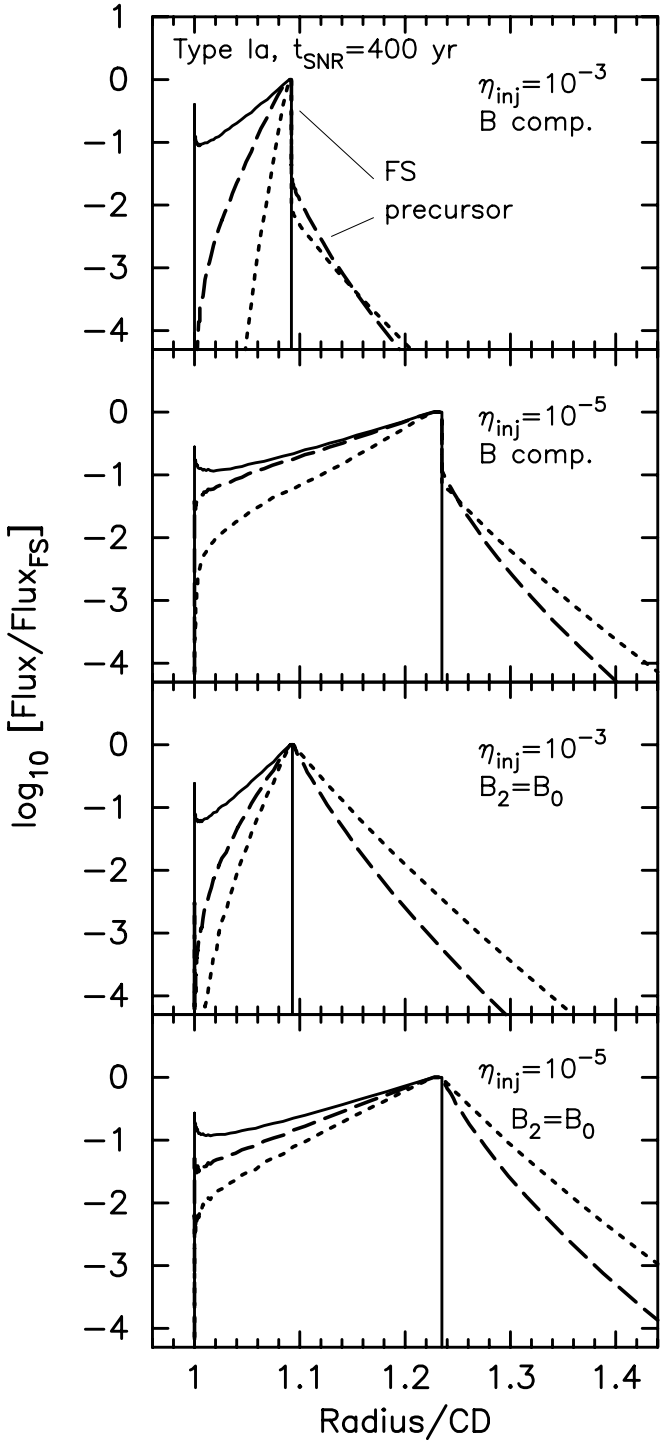

FIG. 3.—Radial synchrotron emission in three energy bands for two magnetic field configurations and two shock injection efficiencies, $\eta_{\rm inj}$. In all panels, the solid line is radio (1–1.4 GHz), the dashed line is low-energy X-rays (0.1–1 keV), and the dotted line is high-energy X-rays (1–10 keV). In the top two panels B is compressed as in eq. (9), while in the bottom two panels $B_2 = B_0$. The flux of each band is normalized to its value at the FS.

2. In the interaction region between the contact discontinuity and the forward shock, the X-ray synchrotron falls off more rapidly than the radio emission. As mentioned in discussing Figure 1, the electrons producing the radio emission suffer only adiabatic losses, while the higher energy electrons producing the X-rays suffer adiabatic losses combined with synchrotron and inverse Compton losses. In Figure 5 we show profiles for the

[8] The results of the CR-hydro model, at early times, depend on the initial conditions, which, unavoidably, are somewhat arbitrary. The initial conditions, in turn, influence the emission at the CD seen in Figs. 3 and 4. For all of the results presented here, the simulation is started at a time $t_0 = 10$ yr with the initial ejecta speed varying linearly with radius from zero to a maximum speed $V^{\rm ej}_{\rm max} = 0.1c$. The initial maximum radius of the ejecta is set by $V^{\rm ej}_{\rm max}$ and t_0, and the early stages of the simulation, and therefore the synchrotron emission at the CD, depend on $V^{\rm ej}_{\rm max}$ and t_0. Of course, the later evolution of the SNR is nearly independent of the starting conditions, as long as the total kinetic energy and ejecta mass stay the same. Since the X-ray emission is dominated by losses at the CD, it is only the radio emission at the CD that depends strongly on $V^{\rm ej}_{\rm max}$ and t_0. For a full discussion of the start-up conditions for the CR-hydro model, see Ellison et al. (2004).

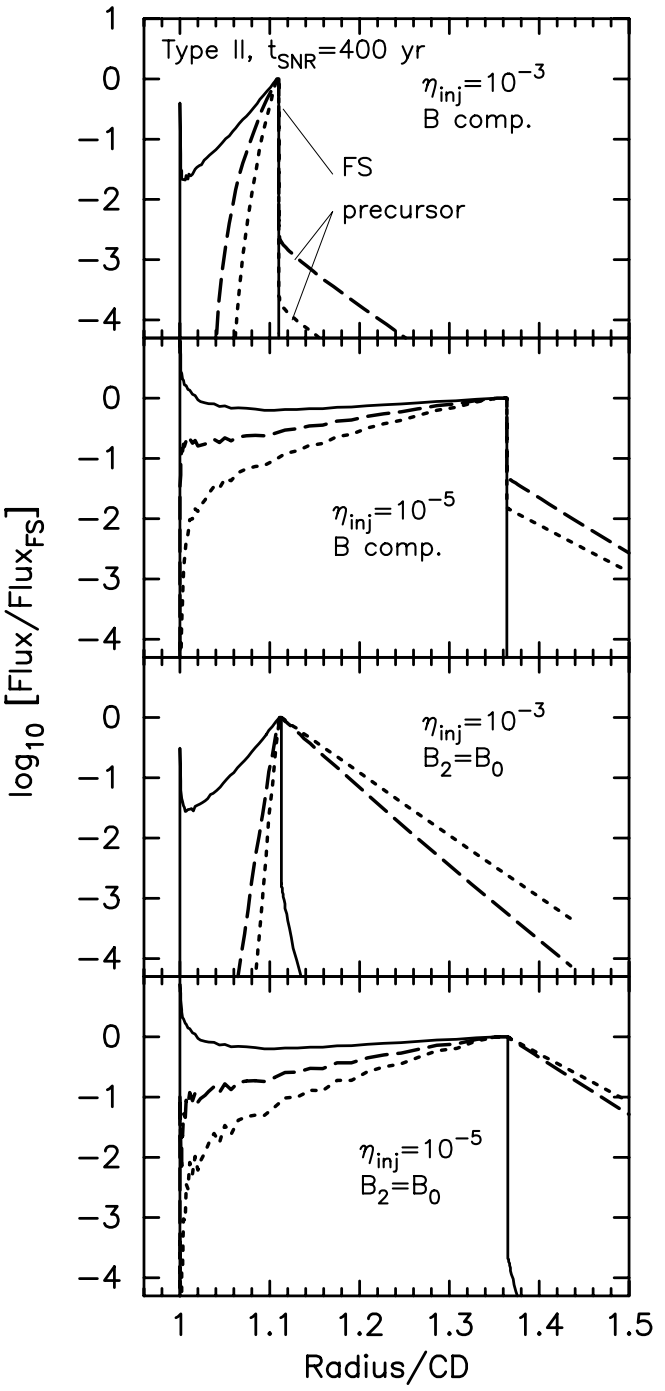

FIG. 4.—Radial synchrotron emission for three energy bands as in Fig. 3 for our Type II SNR prototype.

1–10 keV band with no losses (*solid line*), with just adiabatic losses (*dashed line*), and with adiabatic plus radiative losses (*dotted line*). Since, for typical SNR parameters, the nonthermal X-ray emission comes from the exponential part of the electron spectrum, the X-ray emission will be extremely sensitive to changes in the spectrum coming from any type of loss mechanism.

3. The radio emission can have a secondary peak at the CD, while the X-ray emission, with synchrotron losses, always drops precipitously at the CD. As just mentioned, the radio emission at the CD is sensitive to the starting conditions of the hydro model, but, in any case, the secondary peak is less noticeable in projection as we show below.

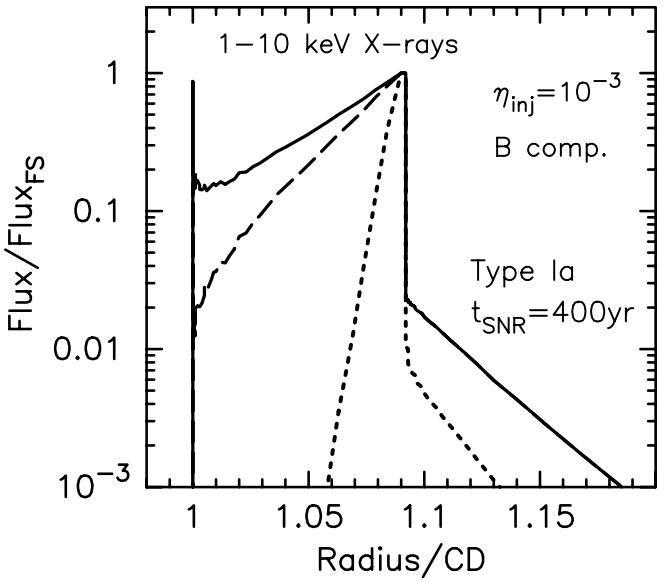

FIG. 5.—Radial synchrotron emission for 1–10 keV X-rays. The dotted line shows the profile with both adiabatic and synchrotron losses included, the dashed line has only adiabatic losses, and the solid line was calculated with no losses. Since there are no adiabatic losses in the precursor, the dashed and solid lines are identical in the precursor.

4. With efficient DSA and a compressed magnetic field (top panels of Figs. 3 and 4), the X-ray falloff is extremely rapid and the X-ray emission can appear as an extremely thin sheet at the FS.

5. The precursor outside of the FS falls slowly if the magnetic field is not compressed at the shock but drops sharply immediately upstream of the shock when B is compressed, with or without efficient DSA (see the top two panels in Figs. 3 and 4). The

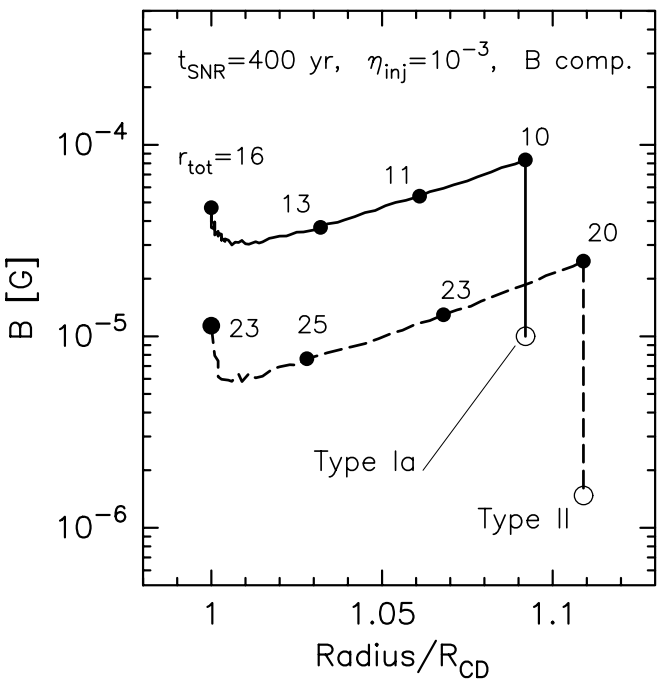

FIG. 6.—Magnetic field strength in the interaction region between the CD and FS for a Type Ia SNR (*solid line*) and a Type II SNR (*dashed curve*). The number above each filled circle is the compression ratio that parcel of gas experienced when it was shocked. The open circles at the ends of the lines indicate the unshocked field at the end of the simulation, i.e., at $t_{SNR} = 400$ yr.

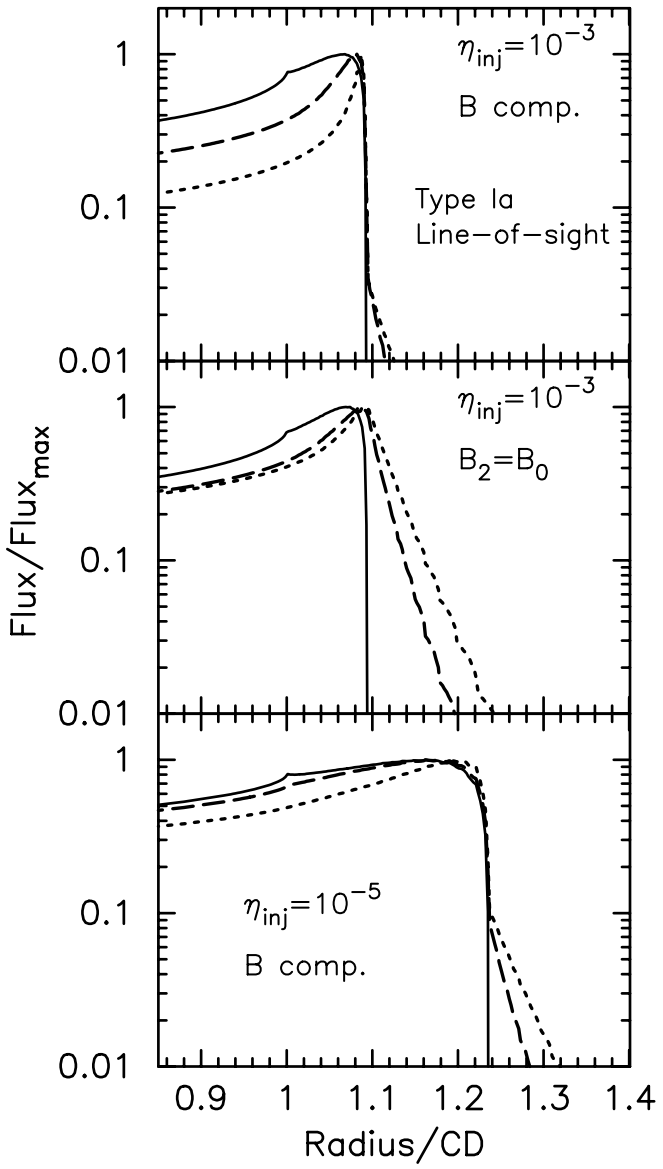

FIG. 7.—Line-of-sight projections for the radial distributions with compressed B shown in Fig. 3. In all panels, the solid line is radio (1–1.4 GHz), the dashed line is low-energy X-rays (0.1–1 keV), and the dotted line is high-energy X-rays (1–10 keV).

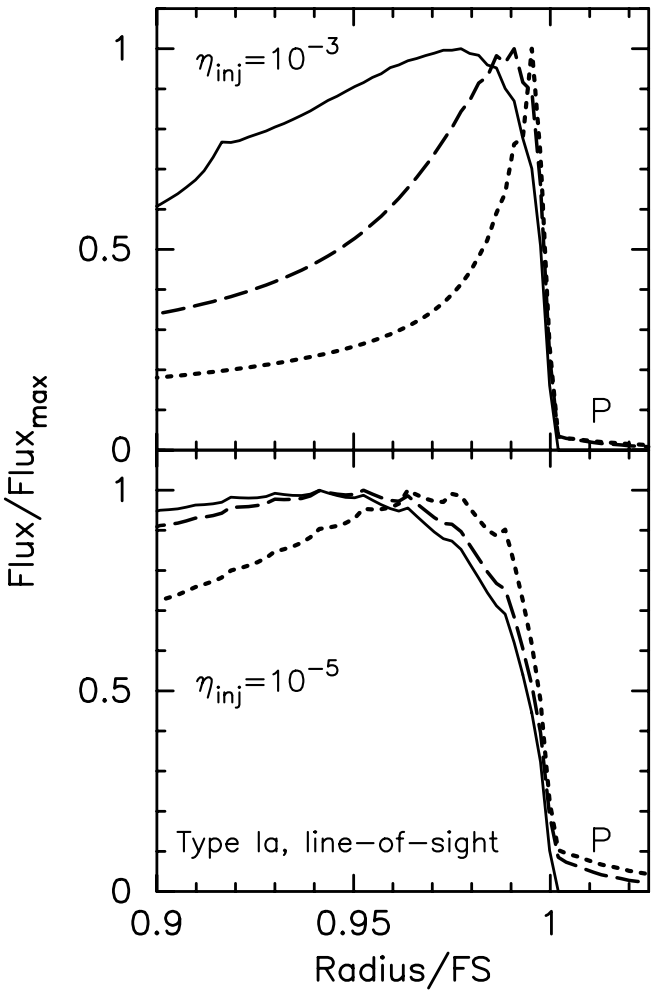

FIG. 8.—Line-of-sight projections for the radial distributions shown in Fig. 3 normalized to the forward shock radius. The magnetic field is compressed in both panels. As in the previous figures, the solid line is radio (1–1.4 GHz), the dashed line is low-energy X-rays (0.1–1 keV), and the dotted line is high-energy X-rays (1–10 keV). Note that the radio emission (*solid lines*) peaks well within the X-ray emission in all cases. The fluctuations, most noticeable in the radio emission for $\eta_{inj}=10^{-5}$, are numerical noise.

sharp drop due to the compressed field will make the X-ray precursor faint and difficult to detect compared to the emission at the FS. Without compression, the precursor should be observable, providing an important diagnostic for the magnetic field structure. Note that the radio precursor has an extremely short upstream diffusion length for all cases and will not be detectable if the diffusive length scale is anywhere near as small as we predict.

6. Comparing the $\eta_{inj}=10^{-3}$ panels against the $\eta_{inj}=10^{-5}$ panels in Figures 3 and 4 shows that the distance between the CD and the FS is nearly a factor of 2 greater in the test particle case than with efficient DSA. Since the limit of the shocked ejecta gives an idea of the position of the CD, R_{FS}/R_{CD} is measurable in several young SNRs with *Chandra* and *XMM-Newton*, making this morphological difference a powerful diagnostic for efficient DSA.

In Figure 6 we show the magnetic field structure, at $t_{SNR}=400$ yr, in the transition region between the CD and FS for our two prototypes with compressed B and $\eta_{inj}=10^{-3}$. The numbers at specific points on the lines indicate the compression ratio, r_{tot}, at the FS at the time that particular parcel of gas was shocked. It is notable that $r_{tot}\gg 4$ in all cases. The difference in r_{tot} between the two models comes about mainly from the lower magnetic field in the pre-SN wind for the Type II model, which results in larger compression ratios. The end of the lines, marked with an open circle, shows the immediate upstream, unshocked magnetic field, B_0, at t_{SNR}. For Type Ia, $B_0=10$ μG and is independent of time, while for Type II, $B_0(r)$ falls off with radius as in equation (1) and at $t_{SNR}=400$ yr is $\simeq 1.5$ μG. A thorough discussion of the influence magnetic field strength has on r_{tot} is given in Ellison et al. (2005).

3.2. *Line-of-Sight Projections*

In Figure 7 we show line-of-sight projections for some of the results shown in Figure 3. Even in projection, it is clear that the radio emission falls off less rapidly behind the FS than the X-ray emission. Projection has little effect on the upstream precursor so the large differences seen in Figure 3 with and without magnetic field compression are similar in projection. The decrease in R_{FS}/R_{CD} for efficient particle acceleration is less obvious in projection, but since the CD generally shows up via thermal X-ray emission, R_{FS}/R_{CD} remains an important diagnostic for the

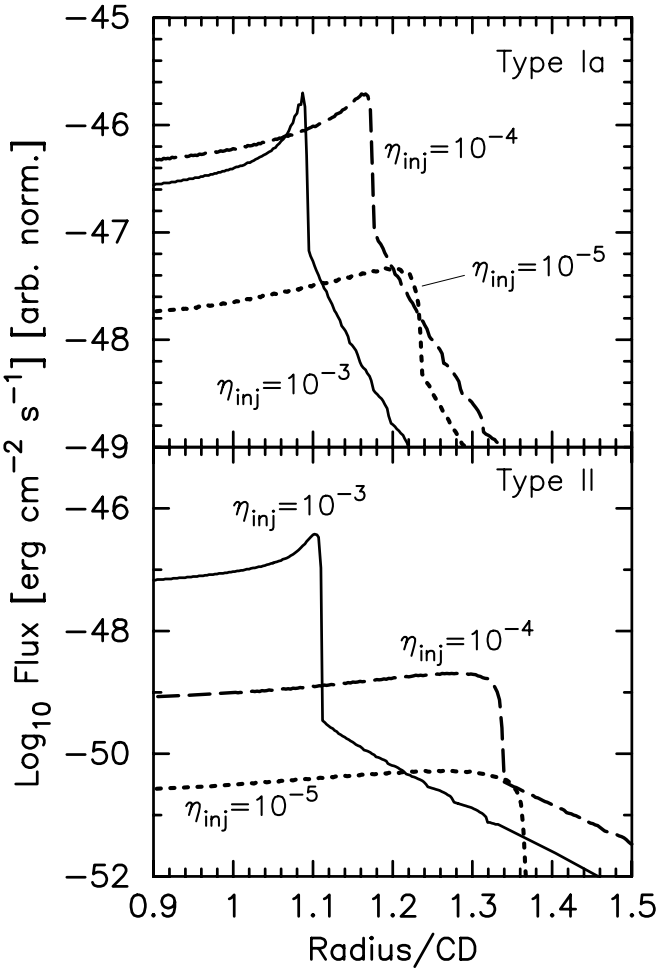

FIG. 9.—Line-of-sight projections for the 1–10 keV X-ray band for various injection efficiencies as marked. All results include magnetic field compression and are for $t_{SNR} = 400$ yr. While the absolute normalization is arbitrary, the relative normalization between the various plots is correct (note the different vertical scales in the two panels).

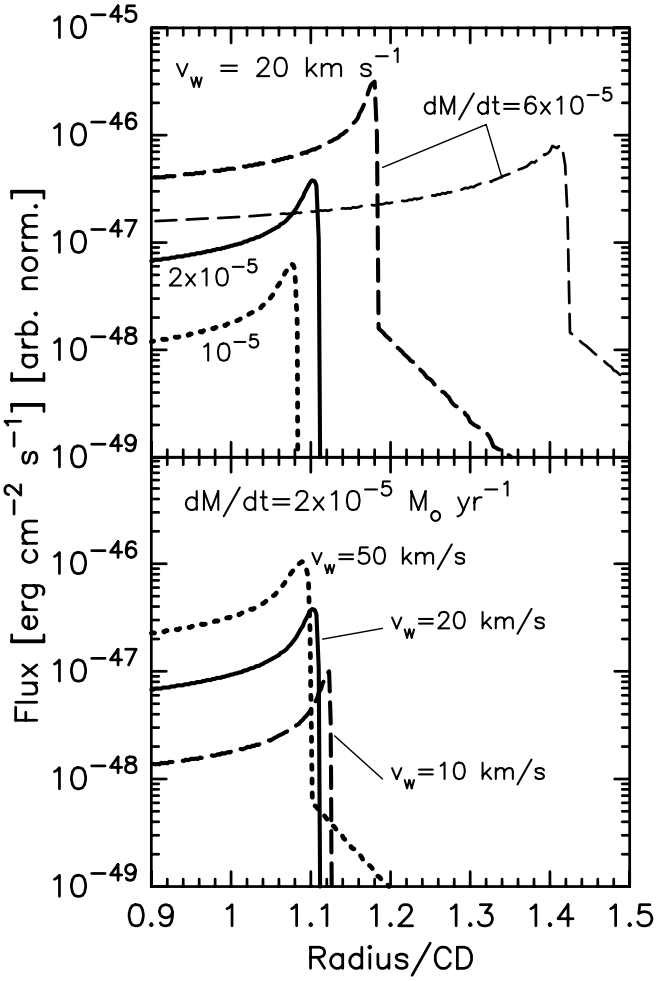

FIG. 10.—Line-of-sight projections for 1–10 keV X-rays for our Type II prototype with compressed magnetic field. The thin dashed line in the top panel has $\eta_{inj} = 10^{-4}$, while all other models shown have $\eta_{inj} = 10^{-3}$. In the top panel, $v_w = 20$ km s^{-1} and dM/dt (in units of $M_\odot$ yr^{-1}) is varied as indicated. In the bottom panel, $dM/dt = 10^{-5}\ M_\odot$ yr^{-1} and v_w is varied. The thin dashed line in the top panel with $\eta_{inj} = 10^{-4}$ has an acceleration efficiency at $t_{SNR} = 400$ yr of more than 70% (similar to that shown in Fig. 12) and demonstrates that values of $R_{FS}/R_{CD} \sim 1.4$, as observed for Cas A, are consistent with efficient DSA in Type II SNe. As in Fig. 9, the absolute normalization is arbitrary, but the relative normalization between the various plots is correct.

presence of efficient CR ion acceleration. Line-of-sight projections of the results shown in Figure 4 are similar.

An important feature that is in the line-of-sight projections and not in the radial profiles is the offset of radio and X-ray peaks at the FS. In Figure 8, the projections for the Type Ia models of Figure 3 with compressed magnetic fields are plotted as a fraction of the FS radius. With or without efficient DSA, the radio peak (*solid line*) occurs inside the X-ray peaks. Behavior such as this is observed in several SNRs including G347 (Lazendic et al. 2004), Kepler (DeLaney et al. 2002), Tycho (Decourchelle et al. 2001), and Cas A (Long et al. 2003). We note, however, that there is another radio peak coincident with the X-ray peak in Tycho (e.g., Dickel et al. 1991). For the efficient acceleration case (*top panel*), the two X-ray peaks are also well separated. Note also that because of projection effects, the maximum emission occurs inside of the FS. As emphasized by Berezhko et al. (2003), care must be taken not to interpret the peak emission as the position of the FS, as done by Bamba et al. (2003) for SN 1006. The actual upstream precursor is indicated in Figure 8 with a "P."

In Figure 9 we compare the line-of-sight 1–10 keV X-ray projections for both Type Ia and Type II prototypes calculated with different DSA injection efficiencies. While the absolute normalization is arbitrary, the lines show the correct relative normalization between the various models and, as expected, the test particle cases with $\eta_{inj} = 10^{-5}$ have lower absolute emissivities. In both panels, the solid lines have $\eta_{inj} = 10^{-3}$, the dashed lines have $\eta_{inj} = 10^{-4}$, the dotted lines have $\eta_{inj} = 10^{-5}$, and all models have magnetic field compression (note the different vertical scales in the two panels). For both SN types, the ratio R_{FS}/R_{CD} increases noticeably as the acceleration becomes less efficient, but R_{FS}/R_{CD} increases somewhat more rapidly for Type II SNRs. Also, for both SN types, the morphology of the X-ray emission varies strongly with η_{inj}: for efficient DSA, there is a pronounced peak at the rim, while the emission is much broader for inefficient DSA. This difference offers another important diagnostic for efficient DSA.

In Figure 10 we keep all parameters of our $\eta_{inj} = 10^{-3}$ Type II model constant except the wind speed, v_w, and the mass-loss rate, dM/dt. In the top panel, $v_w = 20$ km s^{-1} and dM/dt varies, as indicated, and the thin dashed line has $\eta_{inj} = 10^{-4}$; all other lines in Figure 10 have $\eta_{inj} = 10^{-3}$. As dM/dt increases, there is an increase in R_{FS}/R_{CD} indicating, among other things, that self-similarity is no longer a good approximation at $t_{SNR} = 400$ yr. In the bottom panel, $dM/dt = 2 \times 10^{-5}\ M_\odot$ yr^{-1} and v_w is varied as indicated.

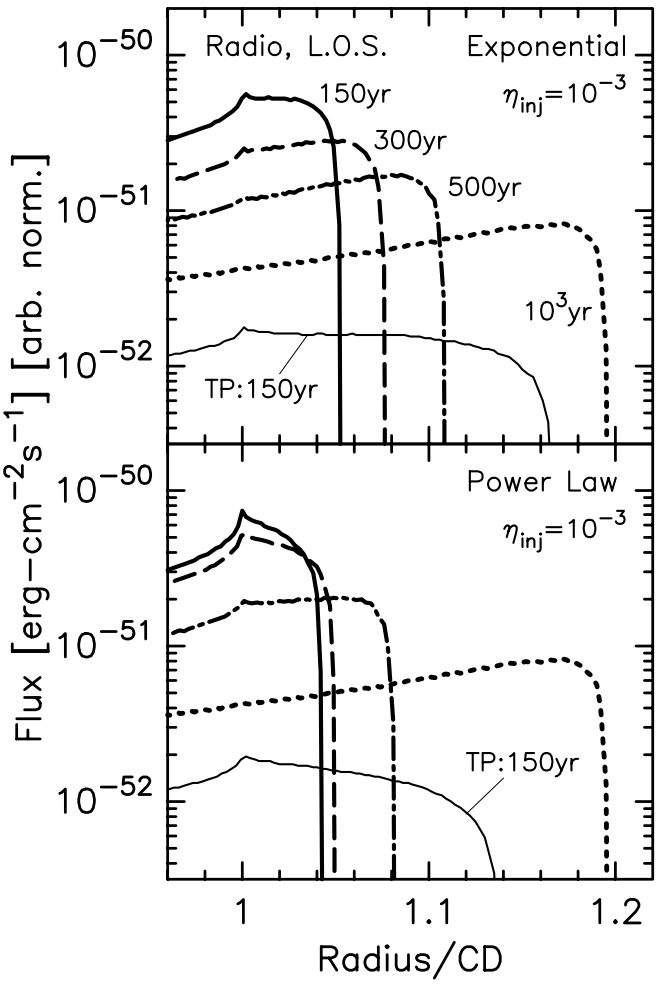

FIG. 11.—Radio synchrotron profiles for our Type Ia prototype at various ages, as indicated, and for an exponential ejecta distribution (*top*) and a power-law ejecta distribution with $n = 9$ (*bottom*). The line styles indicate the same ages in both panels and in all cases, except for the lines marked "TP:150 yr," $\eta_{inj} = 10^{-3}$, and the ambient magnetic field is $B_0 = 10$ μG. As shown by the solid line in the bottom panel, a power-law ejecta distribution produces a radio profile at early times that peaks near the CD. The thin solid lines are test particle results shown for comparison.

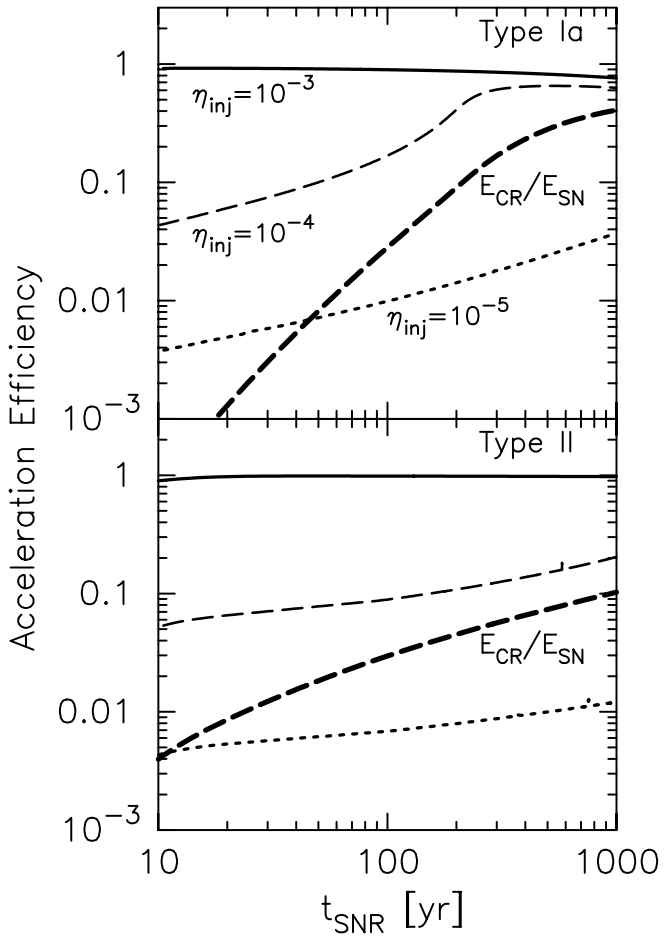

FIG. 12.—*Thin lines*: Shock acceleration efficiencies for our two SN prototypes for various η_{inj}, as indicated. *Thick dashed lines*: Fractions of total SN explosion energy going into CRs for the case where $\eta_{inj} = 10^{-4}$. The line styles indicate the same values of η_{inj} in both panels.

Now, the profiles are relatively insensitive to the changes in v_w, suggesting that self-similarity does apply.

In considering Figures 9 and 10, it is important to note that while R_{FS}/R_{CD} is reduced substantially with efficient CR production in Type Ia SNRs, values of $R_{FS}/R_{CD} > 1.3$ can occur in Type II SNRs with very efficient DSA. The acceleration efficiency for the $\eta_{inj} = 10^{-4}$ model in Figure 10 (*thin dashed line*) is greater than 50% over most of its 400 yr lifetime. This may be relevant for remnants like Cas A and 1E 0102.2−7219, which show $R_{FS}/R_{CD} \sim 1.4$.

3.3. *Radio Emission versus Ejecta Profile and Age*

It is well known that young SNRs with power-law ejecta and power-law ambient medium density profiles have self-similar solutions if CR production is absent or unimportant (e.g., Chevalier 1982a, 1982b). This will be true for the efficient production of CRs as well if the CR production is time invariant (Chevalier 1983). If nonlinear DSA occurs and the acceleration efficiency varies with time, the self-similarity is broken (see Ellison et al. 2004), as is the case with an exponential ejecta density distribution (e.g., Dwarkadas 2000), or for a power-law ejecta distribution once the reverse shock enters the plateau region of the ejecta.

In Figure 11 we show radio emission profiles at various t_{SNR} for Type Ia models with $\eta_{inj} = 10^{-3}$ having exponential (*top panel*) and power-law (*bottom panel*) ejecta density profiles. In self-similar evolution, the ratio R_{FS}/R_{CD} remains constant and this is approximately the case for a power-law ejecta density profile for $t_{SNR} \lesssim 300$ yr. At later times, the self-similarity is broken, as is the case at all times for exponential ejecta density profiles. The thin solid lines are test particle profiles at 150 yr for comparison.

Besides R_{FS}/R_{CD}, the structure of the radio emission in the interaction region between the CD and the FS depends on the assumed ejecta distribution and on the age of the SNR. At early times for the power-law case (*solid line*, *bottom panel of* Fig. 11), the radio emission peaks near the contact discontinuity. This result is consistent with the self-similar model described in Cassam-Chenaï et al. (2005) but, as discussed above, depends somewhat on the starting conditions of the CR-hydro model. At later times the emission drops inside the FS and, as expected, the details of the ejecta profile cease to be important. The lines for 1–10 keV X-rays are not shown, but due to radiative losses and contrary to the radio, they peak strongly just behind the FS for all t_{SNR} as shown in Figure 8.

3.4. *Acceleration Efficiency*

In Figure 12 we show the acceleration efficiency, i.e., the fraction of energy flux crossing the shock that goes into relativistic

ions (see eq. [13] of Ellison et al. 2000), for various $\eta_{\rm inj}$ (*thin lines*) and the fraction of total SN explosion energy put into CRs, $E_{\rm CR}/E_{\rm SN}$, for $\eta_{\rm inj} = 10^{-4}$ (*thick dashed lines*). These models use our Type Ia and II prototype parameters. For the perhaps extreme case of $\eta_{\rm inj} = 10^{-3}$, the fraction of bulk flow energy flux (in the shock rest frame) that is placed in relativistic ions is >80% during the 1000 yr span shown for both SNR prototypes. Even for $\eta_{\rm inj} = 10^{-4}$, the efficiency is >10% most of the time and more than 10% of the total SN explosion energy can be put into CRs over the 1000 yr lifetime.

Of course, the actual injection efficiency of SNR shocks is uncertain and, as noted by Völk et al. (2003), injection may vary over the surface of the SNR and be significantly less where the magnetic field is highly oblique (for a discussion of parallel vs. oblique shock geometry in SN 1006 see Rothenflug et al. 2004). Völk et al. (2003) estimate that to supply the galactic CR population the overall efficiency need only be ~20% of the maximum values obtained by DSA. Dorfi (1990) and Berezhko et al. (1996) obtained similar values. Nevertheless, if the shocks in SNRs accelerate CR *ions* this efficiently via diffusive shock acceleration, clear signatures of the acceleration will be present in the radiation produced by *electrons*.

4. DISCUSSION

4.1. *Narrow Interaction Region*

Perhaps the most unambiguous indication of efficient CR production in SNRs is an interaction region between the contact discontinuity and the forward shock that is considerably narrower than predicted without efficient acceleration (e.g., Blondin & Ellison 2001). While the ratio $R_{\rm FS}/R_{\rm CD}$ depends on various parameters, efficient DSA can easily result in the FS being less than half the distance ahead of the CD predicted with test particle acceleration (see Figs. 3, 4, and 9). This may explain observations of $R_{\rm FS}/R_{\rm CD}$ that are considerably less than the smallest value predicted by test particle, self-similar models, as is the case for Tycho's (e.g., Reynoso et al. 1997; Decourchelle et al. 2001) and Kepler's (e.g., DeLaney et al. 2002; Cassam-Chenaï et al. 2004b) SNRs.

Even in SNRs such as Cas A and 1E 0102.2−7219 in the Small Magellanic Cloud (e.g., Gotthelf et al. 2001; Gaetz et al. 2000; Hughes et al. 2000), where the FS and CD are well separated, DSA may be quite efficient. As shown in Figures 9 and 10, moderately efficient acceleration and/or the presence of a pre-SN wind can result in $R_{\rm FS}/R_{\rm CD} \gtrsim 1.3$. Thus, while the observation of $R_{\rm FS}/R_{\rm CD} = 1.0-1.1$ can be explained naturally if CR ions are being produced efficiently in Type Ia SNe, larger values of $R_{\rm FS}/R_{\rm CD}$ do not necessarily exclude efficient acceleration but may be representative of Type II SNe with pre-SN winds.

4.2. *Precursor and Small-Scale Structure*

In some SNRs extremely small spatial scales in X-ray emission are observed at the FS. Using *Chandra* observations, Long et al. (2003) and Bamba et al. (2003) have independently examined emission profiles in several thin filaments in projection in the northeast shell of SN 1006 that show scale lengths as short as 0.04 pc (assuming a distance to the SNR of ~2 kpc).

In Figure 13 we compare our Type Ia prototype model with $\eta_{\rm inj} = 10^{-3}$ to the SN 1006 observations. We represent the observations with dashed lines that roughly span the maximum and minimum scale heights determined by Bamba et al. (2003, see their Table 4). Even though we have not attempted a detailed fit to SN 1006, it is clear that our compressed B model (*solid line*) matches the overall observations quite well and the shortest scale heights are extremely well modeled. As emphasized by Berezhko et al. (2003), the shortest scale heights occur inside the forward shock and are produced by projection effects when B is compressed and there is a sharp drop in emissivity behind the shock. The actual upstream precursor (indicated with a "P" in Fig. 13) has a much longer scale height as expected from TeV electrons but is not easily discernible with *Chandra* against background emission.

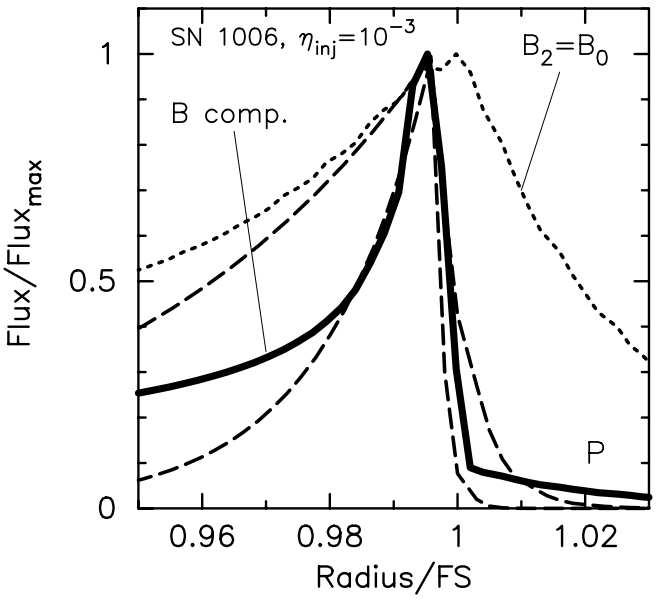

FIG. 13.—Comparison of X-ray line-of-sight profiles from the CR-hydro model with *Chandra* observations of SN 1006. The dashed lines roughly span the maximum and minimum scale heights determined by Bamba et al. (2003) where they assumed exponential profiles. Using their Table 4, we set the maximum (minimum) upstream scale height to be 3″ (1″) and the downstream maximum (minimum) scale height to be 30″ (10″) (the radius of SN 1006 is about 0°.25). The solid line is the X-ray emission in the 1.2–2 keV band using our compressed B model, and for comparison we show (*dotted line*) the 1.2–2 keV band without compressing the field. We have positioned the peaks of the dashed lines to match the solid line.

While our efficient acceleration model with compressed B fits quite well, our uncompressed model (*dotted line*) clearly does not fit, nor does a test particle model (not shown), as is clear from examining the bottom panel of Figure 7. As far as we can tell, our results are in complete agreement with those of Berezhko et al. (2003; see also Ballet 2005) and provide convincing evidence for highly compressed magnetic fields and efficient DSA.

4.3. *Adiabatic and Synchrotron Losses and the Offset of Radio and X-Ray Peaks*

Nonthermal X-ray emission in a fixed energy band is very sensitive to both adiabatic and radiative losses. For typical SNR parameters, synchrotron X-rays are produced in large part by the exponential tail of the electron distribution. Therefore, any energy loss results in a large drop in emissivity. This contrasts with the adiabatic losses of the electrons producing radio emission. Since radio is produced by lower energy electrons in the power-law portion of the distribution rather than the exponential part, emission in a fixed energy band is less sensitive to adiabatic losses. If nonlinear effects from efficient DSA are important, the fixed band radio is even less affected by adiabatic losses since the portion of the electron distribution producing radio is likely to be concave, i.e., flattening with increasing energy.

The synchrotron loss rate will be greater if the magnetic field is compressed at the shock and, therefore, will depend on the

acceleration efficiency. As we show in Cassam-Chenaï et al. (2005) and in Figure 9 here, the morphology of the X-ray emission near the FS varies noticeably with $\eta_{\rm inj}$, peaking more strongly as the acceleration efficiency increases since electrons lose energy before convecting far downstream. This feature provides an important diagnostic for acceleration efficiency.

A direct consequence of X-ray–emitting electrons suffering more losses than radio-emitting ones is an offset in the peak emission of the projected flux at the FS. As shown in Figure 8, the radio emission peaks well within the X-ray emission. The separation will depend on the acceleration efficiency since, for a given set of SN parameters, models with efficient DSA have larger compression ratios and larger downstream magnetic fields. The larger the field, the sharper is the drop in X-ray emission behind the shock, and the closer to the FS position will be the peak X-ray emission.

5. CONCLUSIONS

We have presented a detailed discussion of the influence of efficient diffusive shock acceleration on the radial profiles of synchrotron emission in young SNRs. The evidence that collisionless shocks, in general, can accelerate particles with high efficiency is convincing. There are direct spacecraft observations confirming it (e.g., Eichler 1981; Blandford & Eichler 1987; Ellison et al. 1990; Baring et al. 1997; Shimada et al. 1999), plasma simulations show efficient acceleration consistent with spacecraft observations (e.g., Scholer et al. 1992; Ellison et al. 1993; Giacalone et al. 1997), Galactic CR energetics and composition suggest it (e.g., Axford 1982; Ellison et al. 1997), and theoretical models certainly allow it (e.g., Axford et al. 1978; Drury 1983; Ellison & Eichler 1984; Jones & Ellison 1991; Berezhko et al. 1996; Malkov & Drury 2001; Kang et al. 2002; Blasi 2002). An unresolved question, of course, is whether or not shock acceleration is efficient in SNRs. If DSA is as efficient in accelerating *ions* as suggested, the acceleration process will be nonlinear and will noticeably modify the SNR structure and evolution. We have shown for typical Type Ia and Type II SN parameters that these structural changes, most important of which is the increased shock compression, produce clear signatures in the synchrotron radiation emitted by *electrons*. We note, incidentally, that signatures in the thermal emission may also be present since the energy that goes into relativistic ions comes out of the bulk thermal plasma and produces a drastic reduction in the temperature of the shocked gas (e.g., Decourchelle et al. 2000; Hughes et al. 2000; Ellison et al. 2004).

Of course, our assertion that the nonlinear effects seen in the structure of SNRs are evidence for the efficient acceleration of ions rather than electrons depends on how the energy of shock-accelerated particles is distributed between electrons and ions. While no definitive theory exists describing this partition, the source of the energy going into superthermal particles is the bulk kinetic energy of the converging upstream and downstream plasmas. Diffusive shock acceleration occurs, at its most basic level, when particles diffuse across the shock and scatter nearly elastically off the converging plasmas on either side of the shock. When particles are accelerated from the thermal background, this process favors heavy particles and it is generally assumed that shocks put far more energy into ions than electrons. There is direct evidence for this disparity in acceleration efficiency at the low Mach number shocks that have been studied in the heliosphere (e.g., Feldman 1985; Shimada et al. 1999; see also Ellison et al. 1994), but there is no direct evidence, one way or the other, in the much stronger shocks that exist outside of the heliosphere. Nevertheless, with some confidence, we believe that the structural changes we have discussed are produced by ion acceleration with the radiating electrons being passive markers of the effect.[9]

While direct evidence for the production of CR ions in SNRs would be the observation of a pion-decay spectral feature in GeV–TeV γ-rays, such γ-rays are difficult to detect with the significance necessary to distinguish a pion-decay feature from inverse Compton or bremsstrahlung radiation. Furthermore, in low-density regions, inverse Compton may outshine pion-decay emission, leaving the question of CR ion production for these SNRs open regardless of the sensitivity of γ-ray telescopes. The best chance of seeing a strong pion-decay signal is when a SNR interacts with a dense medium such as the synchrotron-dominated SNR RX J1713.7−3946 (G347.3−0.5) interacting with molecular clouds (see Cassam-Chenaï et al. 2004a and references therein). HESS (High Energy Stereoscopic System) has recently measured, with high significance, the 1–10 TeV energy spectrum in this remnant (Aharonian et al. 2004) and in SNR RX J0852.0−4622 (Aharonian et al. 2005), and while pion decay is certainly the most likely emission mechanism, it is not possible, based on TeV emission alone, to reliably determine the different γ-ray components in these spectra. It should now be possible to test for pion-decay emission using the morphology since HESS has, for the first time, produced γ-ray images of these remnants, and the morphology of inverse Compton and pion decay should be quite different. Observations in the MeV range by GLAST should help significantly to distinguish pion decay from lepton emission and may provide incontrovertible evidence for or against SNRs as the source of CR ions.

We have emphasized here that another signature of efficient CR ion production is the large reduction in the ratio of the radius of the forward shock to the radius of the contact discontinuity, $R_{\rm FS}/R_{\rm CD}$. If a large fraction of the shock energy goes into relativistic particles and high-energy particles that escape from the shock system, $r_{\rm tot} \gg 4$ and the interaction region between the CD and FS will be denser and $R_{\rm FS}/R_{\rm CD}$ will be smaller than with inefficient acceleration (Figs. 3, 4, and 9). This effect may explain observations of $R_{\rm FS}/R_{\rm CD} \sim 1$ in Tycho's and Kepler's SNRs. Type II SNe with pre-SN winds may experience efficient DSA yet still show large $R_{\rm FS}/R_{\rm CD} \sim 1.3-1.4$, consistent with observations of Cas A and 1E 0102.2−7219 (Figs. 9 and 10). While complicating factors such as an irregular ambient medium, dense knots, thin sheets of emission, etc., exist in all SNRs, efficient DSA offers a natural explanation for this important aspect of SNR morphology. Just as important, a large value of $R_{\rm FS}/R_{\rm CD}$ observed in a Type Ia SNR is strong evidence against efficient DSA.

Yet another sign of efficient DSA is the presence of short scale heights seen in nonthermal X-ray emission. Short scale heights are predicted with efficient DSA because the shock will strongly compress the downstream magnetic field and synchrotron losses will lower the emissivity immediately behind the FS. This results in several related morphological effects. First, thin sheets of X-ray emission (e.g., Fig. 9) should be common at the FS, as is consistent with observations. Second, projection effects should result in the distinct separation of the radio and X-ray peaks (e.g., Fig. 8),

[9] We note that so-called shock surfing has been suggested by a number of workers as an effective way of transferring shock energy into electrons (see, e.g., Hoshino & Shimada 2002 and references therein). A thorough discussion of this mechanism is beyond the scope of this paper, but we note that while some descriptions of this effect show large energy gains by electrons, nonlinear effects are almost certain to limit the effectiveness of this process (see Scholer et al. 2003), particularly in the strong shocks we envision for young SNRs.

also commonly observed. Finally, as we show in Figure 13, the short scale heights seen in SN 1006 (e.g., Bamba et al. 2003) are most naturally explained as sharply peaked emission behind the FS seen in projection (Berezhko et al. [2003] have already concluded this for SN 1006). The actual upstream precursor has a long scale length, as expected for TeV electrons, but is weak enough to avoid detection.

SN 1006 seems a clear case where the efficient production of CR ions is taking place, but remnants such as Tycho's and Kepler's, with $R_{\rm FS}/R_{\rm CD} \sim 1$, are also likely candidates. The presence of a significant population of CR ions in young SNRs produces effects that are readily observable in radiation produced by electrons, and we have made predictions, capable of being tested with *Chandra* and *XMM-Newton*, to test this assertion.

The authors are grateful to A. Decourchelle and J. Ballet for the discussions preceding this paper. D. C. E. wishes to acknowledge the International Space Science Institute (ISSI) in Bern, Switzerland for hosting a series of workshops where some of the work presented here was done, as well as support from an NSF grant (INT-0128883) and NASA grant (ATP02-0042-0006).

REFERENCES

Aharonian, F. A., et al. 2004, Nature, 432, 75
———. 2005, A&A, 437, L7
Arnett, D. W. 1988, ApJ, 331, 377
Axford, W. I. 1982, in Proc. 17th Int. Cosmic Ray Conf. (Paris), 155
Axford, W. I., Leer, E., & Skadron, G. 1978, in Proc. 15th Int. Cosmic Ray Conf. (Plovdiv), 132
Ballet, J. 2005, Space Sci. Rev., in press (astro-ph/0503309)
Bamba, A., Yamazaki, R., Ueno, M., & Koyama, K. 2003, ApJ, 589, 827
Baring, M. G., Ellison, D. C., Reynolds, S. P., Grenier, I. A., & Goret, P. 1999, ApJ, 513, 311
Baring, M. G., Ogilvie, K. W., Ellison, D. C., & Forsyth, R. J. 1997, ApJ, 476, 889
Bell, A. R., & Lucek, S. G. 2001, MNRAS, 321, 433
Berezhko, E. G., & Ellison, D. C. 1999, ApJ, 526, 385
Berezhko, E. G., Elshin, V. K., & Ksenofontov, L. T. 1996, Astron. Rep., 40, 155
Berezhko, E. G., Ksenofontov, L. T., & Völk, H. J. 2002, A&A, 395, 943
———. 2003, A&A, 412, L11
Blandford, R., & Eichler, D. 1987, Phys. Rep., 154, 1
Blasi, P. 2002, Astropart. Phys., 16, 429
Blasi, P., Gabici, S., & Vannoni, G. 2005, MNRAS, 361, 907
Blondin, J. M., & Ellison, D. C. 2001, ApJ, 560, 244
Cassam-Chenaï, G., Decourchelle, A., Ballet, J., & Ellison, D. C. 2005, A&A, submitted (astro-ph/0507194)
Cassam-Chenaï, G., Decourchelle, A., Ballet, J., Sauvageot, J.-L., Dubner, G., & Giacani, E. 2004a, A&A, 427, 199
Cassam-Chenaï, G., et al. 2004b, A&A, 414, 545
Chevalier, R. A. 1982a, ApJ, 258, 790
———. 1982b, ApJ, 259, L85
———. 1983, ApJ, 272, 765
Chevalier, R. A., & Luo, D. 1994, ApJ, 421, 225
Chevalier, R. A., & Oishi, J. 2003, ApJ, 593, L23
Decourchelle, A., Ellison, D. C., & Ballet, J. 2000, ApJ, 543, L57
Decourchelle, A., et al. 2001, A&A, 365, L218
DeLaney, T., Koralesky, B., Rudnick, L., & Dickel, J. R. 2002, ApJ, 580, 914
Dickel, J. R., van Breugel, W. J. M., & Strom, R. G. 1991, AJ, 101, 2151
Dorfi, E. A. 1990, A&A, 234, 419
Drury, L. O. 1983, Rep. Prog. Phys., 46, 973
Dwarkadas, V. V. 2000, ApJ, 541, 418
Dwarkadas, V. V., & Chevalier, R. A. 1998, ApJ, 497, 807
Eichler, D. 1981, ApJ, 247, 1089
Ellison, D. C. 2000, in AIP Conf. Proc. 528, Acceleration and Transport of Energetic Particles Observed in the Heliosphere, ed. R. A. Mewaldt et al. (New York: AIP), 383
Ellison, D. C., Berezhko, E. G., & Baring, M. G. 2000, ApJ, 540, 292
Ellison, D. C., Decourchelle, A., & Ballet, J. 2004, A&A, 413, 189
———. 2005, A&A, 429, 569
Ellison, D. C., Drury, L. O., & Meyer, J. 1997, ApJ, 487, 197
Ellison, D. C., & Eichler, D. 1984, ApJ, 286, 691
Ellison, D. C., Giacalone, J., Burgess, D., & Schwartz, S. J. 1993, J. Geophys. Res., 98, 21085
Ellison, D. C., Moebius, E., & Paschmann, G. 1990, ApJ, 352, 376
Ellison, D. C., et al. 1994, PASP, 106, 780
Feldman, W. C. 1985, in Collisionless Shocks in the Heliosphere: Reviews of Current Research, ed. B. T. Tsurutani & R. G. Stone (Geophys. Monogr. 35; Washington, DC: AGU), 195
Gaetz, T. J., Butt, Y. M., Edgar, R. J., Eriksen, K. A., Plucinsky, P. P., Schlegel, E. M., & Smith, R. K. 2000, ApJ, 534, L47
Giacalone, J., Burgess, D., Schwartz, S. J., Ellison, D. C., & Bennett, L. 1997, J. Geophys. Res., 102, 19789
Gotthelf, E. V., Koralesky, B., Rudnick, L., Jones, T. W., Hwang, U., & Petre, R. 2001, ApJ, 552, L39
Hillas, A. M. 2005, J. Phys. G, 31, 95
Hoshino, M., & Shimada, N. 2002, ApJ, 572, 880
Hughes, J. P., Rakowski, C. E., & Decourchelle, A. 2000, ApJ, 543, L61
Jones, F. C., & Ellison, D. C. 1991, Space Sci. Rev., 58, 259
Kang, H., Jones, T. W., & Gieseler, U. D. J. 2002, ApJ, 579, 337
Laming, J. M., & Hwang, U. 2003, ApJ, 597, 347
Lazendic, J. S., Slane, P. O., Gaensler, B. M., Reynolds, S. P., Plucinsky, P. P., & Hughes, J. P. 2004, ApJ, 602, 271
Long, K. S., Reynolds, S. P., Raymond, J. C., Winkler, P. F., Dyer, K. K., & Petre, R. 2003, ApJ, 586, 1162
Malkov, M. A., & Drury, L. 2001, Rep. Prog. Phys., 64, 429
Reynolds, S. P. 1998, ApJ, 493, 375
Reynolds, S. P., & Chevalier, R. A. 1981, ApJ, 245, 912
Reynoso, E. M., Moffett, D. A., Goss, W. M., Dubner, G. M., Dickel, J. R., Reynolds, S. P., & Giacani, E. B. 1997, ApJ, 491, 816
Rothenflug, R., Ballet, J., Dubner, G., Giacani, E., Decourchelle, A., & Ferrando, P. 2004, A&A, 425, 121
Scholer, M., Shinohara, I., & Matsukiyo, S. 2003, J. Geophys. Res., 108, 4
Scholer, M., Trattner, K. J., & Kucharek, H. 1992, ApJ, 395, 675
Shimada, N., Terasawa, T., Hoshino, M., Naito, T., Matsui, H., Koi, T., & Maezawa, K. 1999, Ap&SS, 264, 481
Völk, H. J., Berezhko, E. G., & Ksenofontov, L. T. 2003, A&A, 409, 563
Völk, H. J., Berezhko, E. G., Ksenofontov, L. T., & Rowell, G. P. 2002, A&A, 396, 649